

Dielectric function of cubic InN from the mid-infrared to the visible spectral range

P Schley¹, R Goldhahn¹, C Napierala¹, G Gobsch¹, J Schörmann²,
D J As², K Lischka², M Feneberg³ and K Thonke³

¹ Institute of Physics and Institute of Micro- and Nanotechnologies, Technical University of Ilmenau, PF 100565, 98684 Ilmenau, Germany

² Department of Physics, University of Paderborn, Warburger Straße 100, 33098 Paderborn, Germany

³ Institute of Semiconductor Physics, University of Ulm, 89069 Ulm, Germany

E-mail: pascal.schley@tu-ilmenau.de

Received 13 November 2007, in final form 17 January 2008

Published 26 March 2008

Online at stacks.iop.org/SST/23/055001

Abstract

The complex dielectric function for cubic InN is determined by spectroscopic ellipsometry from the mid-infrared into the visible spectral region. Films were grown by molecular beam epitaxy on c-GaN/3C-SiC pseudo-substrates. The high electron densities above 10^{19} cm^{-3} cause pronounced Burstein–Moss shifts at the gap. Taking into account the non-parabolicity and the filling of the conduction band, data analysis yields renormalized band edges between 0.43 and 0.455 eV. Including carrier-induced band-gap renormalization, we estimate a zero-density band gap of ~ 0.595 eV for c-InN which is about 85 meV lower than for hexagonal InN. Values for the electron effective mass, the static and high-frequency dielectric constant are reported.

(Some figures in this article are in colour only in the electronic version)

1. Introduction

Recent spectroscopic ellipsometry (SE) [1, 2] and absorption [3, 4] studies emphasized a low band gap E_0 for hexagonal (h-)InN. Zero-density values at room temperature (RT) between 0.65 [1, 4] and 0.68 eV [2, 3] were reported. The small differences are attributed to the use of different approaches for modeling the spectral dependence around the absorption edge and whether carrier-induced band-gap renormalization (BGR) and Burstein–Moss shift (BMS) were taken into account. An additional uncertainty arises from the determination of the bulk electron concentration (N_c) in the presence of a strong surface accumulation layer [5]. The usually employed Hall measurements yield the sheet electron density (including an accumulation layer) only from which, with the knowledge of the layer thickness, a volume concentration is calculated. Optical [1, 6, 7] and electrical [4] studies indicate, however, that N_c in the bulk-like part of the sample is considerably lower than those obtained from the Hall studies.

Much less is known about the properties of the cubic (c-) counterpart. Due to the lack of reliable experimental data, a gap value of 1.8 eV was used in order to determine the

bowing parameter of the cubic $\text{In}_x\text{Ga}_{1-x}\text{N}$ alloy system [8]. Theoretical calculations [9–11] predict, however, that the band gap of c-InN is about 80 to 230 meV lower than for h-InN, i.e., the experimental value should lie in the range between 0.42 and 0.60 eV.

Several attempts were made in the past to grow cubic InN on various substrates such as GaAs (0 0 1) with an InAs buffer layer [12], 3C-SiC [13] or directly on GaAs (0 0 1) [14]. Cubic phase purities of 65% [13] to 82% [14] and photoluminescence (PL) peak energies around 0.7 eV were reported for these films. Only recently high-quality c-InN layers with a considerably reduced fraction of hexagonal inclusions became available, which were deposited on 3C-SiC substrates with a thick c-GaN buffer layer [15]. A parabolic band structure was assumed in order to estimate the carrier concentration of the films for the Stokes shift between PL onset and the absorption edge. The assumption of a BGR of 50 meV led to a band gap of c-InN of 0.56 eV at RT.

In the current paper, we present for the first time SE data for the mid-infrared (MIR) spectral range. The fit of the phonon–plasmon modes allows an accurate determination of the plasma frequency (ω_p) as previously demonstrated for

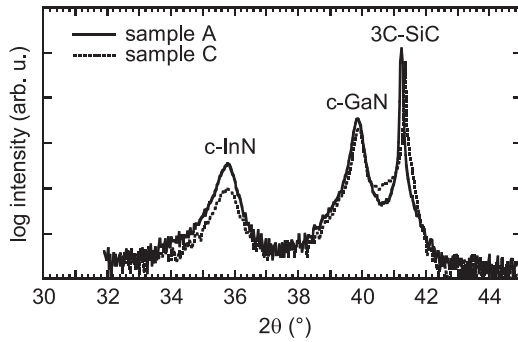


Figure 1. (0 0 2) reflection $\omega - 2\theta$ scans recorded for the InN films with the largest (A) and the smallest (C) layer thicknesses.

h-InN [1] and thus of N_e . With this knowledge and together with the dielectric function (DF) data around the absorption edge, an elaborate analysis of BGR and BMS effects for non-parabolic conduction bands becomes possible allowing a re-evaluation of the zero-density band gap.

2. Experimental details

In a recent paper [15], we have investigated the influence of growth conditions on the structural properties of c-InN films. It was found that the amount of hexagonal inclusions decreases with decreasing growth temperature. Therefore, in order to obtain the optical properties of cubic InN only almost phase pure c-InN samples were investigated in the current paper.

The three c-InN samples were grown on 3C-SiC substrates ($N_e \approx 5 \times 10^{17} \text{ cm}^{-3}$) by rf plasma-assisted molecular beam epitaxy at growth temperatures of 434 °C (sample A), 431 °C (sample B) and 419 °C (sample C). All films were nominally undoped. Prior to the growth of the 127 nm (A), 122 nm (B) and 75 nm (C) thick c-InN layers, ~ 600 nm thick c-GaN buffer layers ($N_e \approx 2 \times 10^{17} \text{ cm}^{-3}$) were deposited.

High-resolution x-ray diffraction measurements were carried out in order to determine the structural properties of the films. Figure 1 shows $\omega - 2\theta$ scans of two samples which differ in the c-InN layer thickness nearly by factor 2. Bragg peaks were found at 35.8°, 39.9° and 41.3° corresponding to c-InN (0 0 2), c-GaN (0 0 2) and 3C-SiC (0 0 2), respectively. As expected, the c-InN peaks become sharper with increasing layer thickness. As shown in [16], the diffraction pattern for sample B is almost identical to results for A. The lattice constants obtained from the $\omega - 2\theta$ -scan are $(5.01 \pm 0.01) \text{ \AA}$, which are in good agreement to other published values of 4.98 Å [17] and 4.986 Å [18], and also with theoretical calculations [10, 19]. Reciprocal space maps were recorded to determine the phase purity of the c-InN layers [15]. The hexagonal fractions for samples A, B and C amount to 11%, 10% and 5%, respectively. These values are some of the lowest reported for c-InN.

Two different ellipsometer setups were applied for data acquisition from the MIR to the visible spectral range. A Fourier-transform-based spectroscopic ellipsometer was used to investigate the optical properties in the MIR range ($350\text{--}2000 \text{ cm}^{-1}$). The spectral resolution of the setup was 1 cm^{-1} .

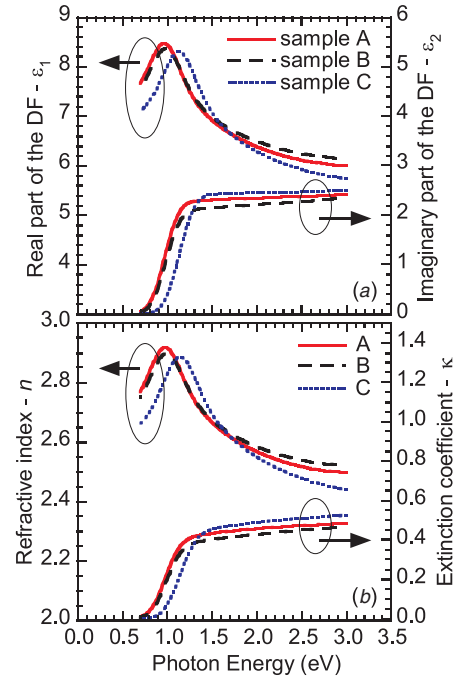


Figure 2. Real and imaginary parts of the complex DF (a) in comparison to which of the complex refractive index (b) for the three cubic InN samples. The carrier-induced Burstein–Moss shift of the onset in ϵ_2 as well as in κ is apparent.

The spectra were measured at room temperature and at angles of incidence of 60°, 65° and 70°. From the near-IR to visible region (0.7–3 eV), the ellipsometric parameters Ψ and Δ were measured by a commercially available rotating-analyzer ellipsometer at RT and at multiple angles of incidence ($\Phi = 62^\circ, 68^\circ$ and 74°). The spectral resolution was 10 meV. The complex DF ($\bar{\epsilon} = \epsilon_1 + i\epsilon_2$) was obtained by fitting the experimental Ψ and Δ data using a multi-layer model c-InN/c-GaN/3C-SiC. Surface roughness in the range of 4–6 nm has taken into account by a Bruggeman effective-medium layer (50% voids in a c-InN matrix) on top. The reliability and accuracy of this approach for obtaining bulk DFs has been demonstrated elsewhere [20]. The PL at 10 K was excited by the 514 nm line of an Ar-ion laser and detected by a liquid-nitrogen cooled InSb photodiode.

3. Results and discussion

Figure 2(a) shows the real (ϵ_1) and the imaginary (ϵ_2) parts of the DF in the vicinity of the band gap for all samples. First, the spectral dependence of ϵ_2 up to 3 eV is very similar to the behavior found for h-InN [21]. We observe a sharp increase of ϵ_2 in the energy range from 0.8 up to 1.3 eV followed by a plateau. The onset of absorption for sample C is shifted by about 160 meV to higher energies in comparison to samples A and B. It indicates that BMS due to band-filling is strongest for sample C while a lower but similar electron concentration is expected for the two other samples. Similar to our results, Kasic *et al* observed a distinct blueshift of the absorption edge with increasing electron concentration for h-InN films [1].

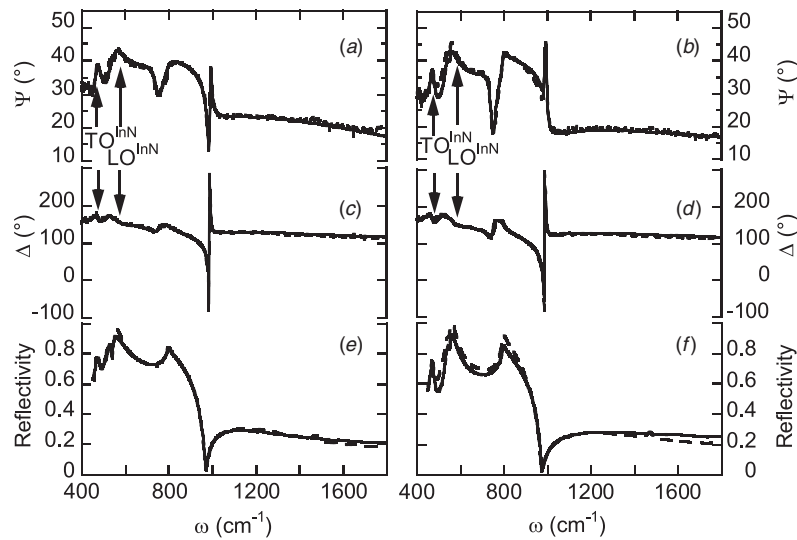


Figure 3. Measured (dashed lines) and modeled (solid lines) Ψ spectra (a) and (b) and Δ spectra (c) and (d) at 65° angle of incidence as well as the IR reflectance spectra (e) and (f) for samples B (left) and C (right). The positions of the TO and LO phonon modes are indicated by arrows.

Table 1. Summary of the determined phonon and plasma frequencies as well as broadening parameters, electron concentrations and mobilities, and high-frequency dielectric constants of c-InN. The average electron effective masses $m^*(N_e)$ are also given.

Sample	ω_{TO} (cm^{-1})	ω_{p} (cm^{-1})	γ_{p} (cm^{-1})	N_e (10^{19}cm^{-3})	μ_e ($\text{cm}^2 \text{V}^{-1} \text{s}^{-1}$)	$\varepsilon_\infty(N_e)$	$m^*(N_e)/m_0$
A	468.9	2025	167	2.1	835	6.97	0.067
B	469.3	2061	190	2.2	720	6.95	0.068
C	470.0	2599	212	3.8	580	6.64	0.076

Secondly, N_e influences also the shape of ε_1 . The peak position shifts due to Kramers–Kronig consistency of ε_1 and ε_2 , and the high-frequency dielectric constant ε_∞ (extrapolation of ε_1 to zero photon energy) becomes sample dependent. In order to obtain this quantity the spectral dependence of ε_1 below the peak maximum has to be fitted. For this range, we applied the analytic formula [22, 23]

$$\varepsilon_1(\hbar\omega) = 1 + \frac{2}{\pi} \left(\frac{A_0 \ln \frac{E_1^2 - (\hbar\omega)^2}{E_G^2 - (\hbar\omega)^2}}{2} + \frac{A_1 E_1}{E_1^2 - (\hbar\omega)^2} \right), \quad (1)$$

which was derived by the Kramers–Kronig transformation of ε_2 which has a constant value A_0 between the effective band gap E_G (roughly corresponding to the absorption edge here) and the delta function at E_1 with magnitude A_1 . The latter summarizes the contributions of all high-energy critical-point transitions [22]. The fit yielded for all samples values of $E_1 = (4.35 \pm 0.22)$ eV, $A_1 = (20.26 \pm 1.13)$ eV and $A_0 = (3.1 \pm 0.1)$ while E_G increases from 0.97 to 1.14 eV from sample A to C, respectively. With these values ε_∞ can be calculated via equation (1) in the case of $\hbar\omega \rightarrow 0$. The determined sample-dependent ε_∞ values are listed in table 1, a clear lowering is found for sample C.

A large number of reports on the determination of the band gap of InN evaluate the spectral dependence of the absorption coefficient (α) determined by transmission measurements. The analysis is based on the fact that α is proportional to

the imaginary part of the DF via the relation $\alpha = \omega \varepsilon_2 / (nc_0)$ (ω is the angular frequency of light; c_0 is the vacuum speed of light). Then, a square-root dependence of α (and thus ε_2) on the photon energy $\hbar\omega$ is assumed (being only valid in the case of parabolic valence and conduction bands) and the spectral dependence of the refractive index n is neglected. Finally, the absorption edge (or band gap) is estimated by extrapolating α^2 to zero. Such an analysis cannot be applied in the present case for the following reasons. (i) Figure 2(b) displays the real (n) and imaginary (κ) parts of the complex refractive index ($\tilde{N} = n + i\kappa$). It clearly emphasizes that n is not constant around the band edge but considerably depends on $\hbar\omega$. Therefore, it is necessary to analyze directly ε_2 around the absorption edge. (ii) Any semiconductor with a low band gap exhibits a characteristic non-parabolicity of the conduction band, i.e. the joint density of states which is the decisive quantity for the spectral behavior of ε_2 and thus α deviates from the square-root dependence. (iii) No analytic formula can be derived for the shape of ε_2 in the case of conduction band filling. However, points (ii) and (iii) can be successfully taken into account by numerical calculation of ε_2 , which was recently demonstrated for h-InN films [2]. Fundamental equations are summarized below.

The most important input parameter for such an analysis is the electron concentration which can be determined from the analysis of the coupled phonon–plasmon modes in the MIR. Figure 3 shows the ellipsometric Ψ (a, b) and Δ (c, d) spectra

of the samples B and C, i.e., typical examples for samples with lower and higher carrier concentration, respectively. For the fit, the DFs in the MIR range of 3C-SiC, c-GaN and c-InN layers were analyzed by applying the widely used formula in which the phonon and free-carrier contributions to the complex DF were described by a factorized model considering the anharmonic coupling effects between free-carrier plasmons and longitudinal-optical (LO) phonons [24, 25]:

$$\bar{\varepsilon}(\omega) = \varepsilon_\infty \frac{\prod_{j=1}^2 (\omega^2 + i\gamma_{LPP,j}\omega - \omega_{LPP,j}^2)}{(\omega^2 + i\gamma_p\omega)(\omega^2 + i\gamma_{TO}\omega - \omega_{TO}^2)}, \quad (2)$$

where $\omega_{LPP,j}$ and $\gamma_{LPP,j}$ are the eigenfrequency and the broadening value of the longitudinal-phonon-plasmon (LPP) modes, respectively. The γ_p values are considered as the plasmon broadening parameters in the long-wavelength limit. ω_{TO} and γ_{TO} are the frequency and the broadening value of the transversal-optical (TO) lattice mode, respectively. The needed ε_∞ values for each c-InN film are taken from table 1. The ω_{LPP} eigenfrequencies are related to all characteristic frequencies via

$$\omega_{LPP,j}^2 = \frac{1}{2} [\omega_{LO}^2 + \omega_p^2 + (-1)^j \sqrt{(\omega_{LO}^2 + \omega_p^2)^2 - 4\omega_p^2\omega_{TO}^2}], \quad (3)$$

where ω_{LO} denotes the frequency of the LO phonon mode. As in previous ellipsometric MIR studies [1], ω_{LO} was kept constant. Here, a value of 588 cm^{-1} was adopted which was obtained from Raman studies of c-InN films [26]. It means that besides the broadening values the ω_p and ω_{TO} frequencies have to be adjustable. Figures 3(a)–(d) demonstrate the excellent agreement between the fit and experimental data for samples B and C. MIR reflectance measurements as shown in figures 3(e) and (f) emphasize the spectral dependence of $\bar{\varepsilon}(\omega)$ according to equation (2). The good accordance of measured and calculated data further confirms the validity of the used model and proofs the quality of our extracted parameters.

The fitted ω_{TO} and ω_p values are summarized in table 1. For the former we get values between 468.9 cm^{-1} and 470.0 cm^{-1} which match well to the Raman results of $\omega_{TO} = 470 \text{ cm}^{-1}$ given in [26]. Determination of the electron concentration and mobility becomes possible from ω_p and γ_p by applying the following equations [27]:

$$\omega_p^2 = \frac{N_e e^2}{\varepsilon_0 \varepsilon_\infty m^*(N_e)} \quad (4)$$

and

$$\mu_e = \frac{e}{m^*(N_e) \gamma_p}, \quad (5)$$

where e is the electrical unity charge, and ε_0 represents the vacuum permittivity. The average effective mass $m^*(N_e)$ accounts for the non-parabolic dispersion of the conduction band (CB) for a low band-gap material, i.e., only the quantity $N_e/m^*(N_e)$ can be directly determined from the plasma frequency [7, 28]. For the further evaluation, $m^*(N_e)$ has to be calculated via [27]

$$\frac{1}{m^*(N_e)} = \frac{1}{12\pi^3 \hbar^2 N_e} \int d\mathbf{k} \frac{\partial^2 E_c(k)}{\partial k^2} f(E_c), \quad (6)$$

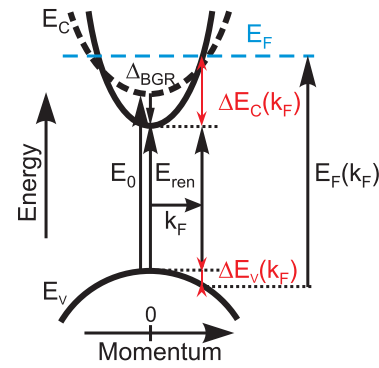


Figure 4. Schematic illustration of the band alignment in the vicinity of the Γ point of the BZ induced by band-gap renormalization Δ_{BGR} and band filling effects $\Delta E_c(k_F)$ and $\Delta E_v(k_F)$ as explained in the text. Note that $E_F(k_F)$ represents the valence-conduction-band spacing at the Fermi wave vector k_F .

where $f(E_c)$ is the Fermi distribution function, and $E_c(k)$ denotes the dispersion of the CB. The integral runs over all occupied states in the CB up to the Fermi energy E_F , this quantity follows from the fit of the $\varepsilon_2(\omega)$ curves as described below.

The whole problem has to be solved self-consistently because the high electron concentration causes a change of the band structure which is illustrated in figure 4. First, carrier-induced band-gap renormalization Δ_{BGR} leads to a renormalized band gap E_{ren} (see figure 4) due to electron–electron (ΔE_{e-e}) and electron-ionized impurity (ΔE_{e-i}) interaction. Appropriate formulae can be found elsewhere [29]. Secondly, the energetic position of Fermi level is located above the CB minimum [$\Delta E_c(k_F)$] as depicted in figure 4. As a consequence, the absorption does not occur at the Γ point (at $k = 0$) of the Brillouin zone (BZ) but at the Fermi wave vector k_F because it requires empty states in the CB. Hence, the energy of the valence band (VB) at k_F is lower in comparison to the Γ point (this quantity is denoted by $\Delta E_v(k_F)$). This means that a small amount of the Burstein–Moss shift ($\Delta E_{cv}(k_F) = \Delta E_c(k_F) - \Delta E_v(k_F) = E_F(k_F) - E_{ren}$) is caused by the curvature of the VB.

So for the evaluation of the BMS the curvature of the CB and VB is needed. The VB dispersion (E_v) can be described by a parabolic approximation with a proposed effective mass for the holes of $m_h = 0.5m_0$ [30]. Since the CB of c-InN is highly non-parabolic we applied the formula given by Kane’s two-band $\mathbf{k} \cdot \mathbf{p}$ model [31] inserting the renormalized band gap ($E_{ren} = E_0 + \Delta_{BGR}$) instead of the fundamental band gap E_0 [2]:

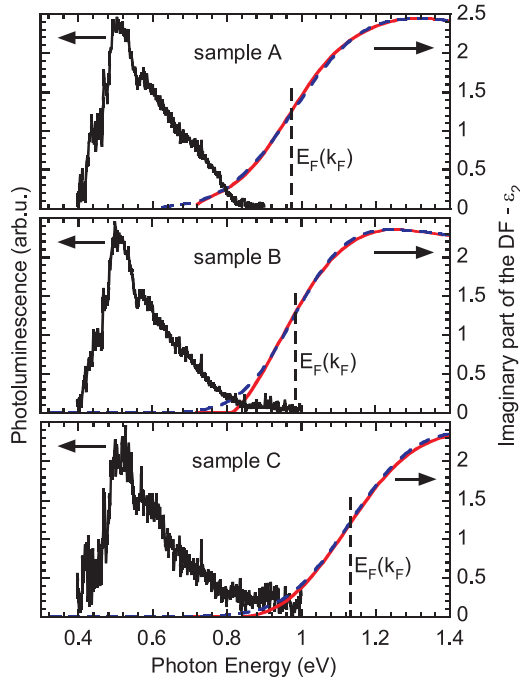
$$E_c(k) = \frac{E_{ren}}{2} + \frac{\hbar^2 k^2}{2m_0} + \frac{1}{2} \sqrt{E_{ren}^2 + 4E_p \frac{\hbar^2 k^2}{2m_0}}. \quad (7)$$

Note that Kamińska *et al* [32] employed a similar approach using the actual band gap instead of E_0 for the investigation of the dependence of InN PL on hydrostatic pressure.

The analysis of the experimental data starts from a calculation of the imaginary part of the DF that is proportional

Table 2. Fermi energies as well as contributions to Burstein–Moss shift and band-gap renormalization used for determining the zero-density band gaps E_0 .

Sample	$E_F(k_F)$ (eV)	$\Delta E_c(k_F)$ (meV)	$\Delta E_v(k_F)$ (meV)	$\Delta E_{cv}(k_F)$ (meV)	E_{ren} (eV)	ΔE_{e-i} (meV)	ΔE_{e-e} (meV)	Δ_{BGR} (meV)	E_0 (eV)
A	0.975	464	−56	520	0.455	−86	−54	−140	0.595
B	0.982	475	−57	532	0.450	−87	−54	−141	0.591
C	1.130	618	−82	700	0.430	−108	−65	−173	0.603

**Figure 5.** Photoluminescence spectrum at $T = 10$ K as well as the calculated shape of the imaginary part of the DF (dashed lines) in comparison to the experimental data (solid lines) for samples A–C.

to the joint density of states via

$$\varepsilon_2(\hbar\omega) \sim \frac{1}{(\hbar\omega)^2} \frac{2}{(2\pi)^3} \int_{BZ} |P_{cv}|^2 [1 - f(E_c)] \times \delta(E_c(k) - E_v(k) - \hbar\omega) d^3k, \quad (8)$$

where P_{cv} is the momentum matrix element. The CB non-parabolicity is taken into account by inserting equation (7) for $E_c(k)$. The integration is carried out in the reciprocal (k) space over the whole BZ, further details can be found elsewhere [2].

A comparison of the calculated and experimental $\varepsilon_2(\omega)$ curves for all three samples is shown in figure 5. Note that with an E_P parameter of 14 eV only E_{ren} and $E_F(k_F)$ (values are given in table 2) were adjusted in order to get the excellent agreement and to match the ω_p values in table 1. The data correspond to electron concentrations between 2.1 and $3.8 \times 10^{19} \text{ cm}^{-3}$ while mobilities between 835 and $580 \text{ cm}^2 \text{ V}^{-1} \text{ s}^{-1}$ are estimated.

It can be seen from table 2 that the renormalized band gaps for the three highly degenerate InN films are nearly identical. We assume similarly to h-InN a temperature-dependent band gap shift of 35–50 meV from RT to 10 K [33]. The onset of

Table 3. Theoretical predicted fundamental band gaps E_0 (in eV) for c-InN and h-InN using equal approximations respectively for both polymorphs in comparison to our experimental findings.

	c-InN	h-InN
Furthmüller <i>et al</i> [10]	0.59	0.82
Rinke <i>et al</i> [9]	0.53	0.72
Bagayoko <i>et al</i> [19]	0.65	–
Briki <i>et al</i> [34]	0.57	–
Persson <i>et al</i> [11]	0.59	0.67
Our work	0.595	0.68 [2]

the low temperature PL spectra in figure 5 is indeed found at approximately these energies. All three samples show nearly the same PL signal furthermore confirming the equality of our extracted renormalized band gaps given in table 2.

Now, the zero-density band gap E_0 can be estimated from E_{ren} and the calculated Δ_{BGR} . The detailed analysis yields 0.595, 0.591 and 0.603 eV for sample A, B and C, respectively, which is slightly higher than the preliminary value of 0.56 eV [15]. For comparison, an E_P of only 10 eV as for h-InN [2, 29] increases E_{ren} up to 100 meV and the difference between the three E_0 values becomes much larger; therefore, a zero-density band gap of 0.595 eV with a corresponding effective electron mass of $0.041 m_0$ at the CB minimum is very likely. Table 3 provides a summary of theoretically calculated band gaps. While in two cases the c-InN and h-InN gaps differ about 200 meV, the results of Persson *et al* agree well with our finding of ~ 85 meV difference.

Finally, the Kramers–Kronig transformation of the calculated $\varepsilon_2(\omega)$ curve for $E_0 = 0.595$ eV leads to an ε_∞ of 7.84 from which one achieves a static dielectric constant ε_r of 12.3 by using the Lyddane–Sachs–Teller relation (for values of ω_{TO} see table 1).

4. Conclusion

We have determined the dielectric function of c-InN layers from the MIR into the visible spectral region. The evaluation of the plasma frequency from IR data provides the electron concentration of the films. We found that the carrier-dependent high-frequency dielectric constant decreases with increasing electron concentration. By taking into account the band-filling effects (BMS, BGR) and non-parabolicity of the conduction band in the analysis of ε_2 in the vicinity of the band gap, we estimate a zero-density c-InN band gap of 0.595 eV which is about 85 meV lower than that for h-InN.

Acknowledgments

The authors would like to thank H Nagasawa and M Abe from HOYA Corporation, SiC Development Center, for supplying the 3C-SiC substrates.

References

- [1] Kasic A, Valcheva E, Monemar B, Lu H and Schaff W J 2004 *Phys. Rev. B* **70** 115217
- [2] Schley P *et al* 2007 *Phys. Rev. B* **75** 205204
- [3] Walukiewicz W, Ager J W III, Yu K M, Liliental-Weber Z, Wu J, Li S X, Jones R E and Denlinger J D 2006 *J. Phys.: Appl. Phys.* **39** R83
- [4] Koblmüller G, Gallinat C S, Bernardis S, Speck J S, Chern G D, Readinger E D, Shen H and Wraback M 2006 *Appl. Phys. Lett.* **89** 071902
- [5] Piper L F J, Veal T D, Mahboob I, McConville C F, Lu H and Schaff W J 2004 *Phys. Rev. B* **70** 115333
- [6] Arnaudov B, Paskova T, Paskov P P, Magnusson B, Valcheva E, Monemar B, Lu H, Schaff W J, Amano H and Akasaki I 2004 *Phys. Rev. B* **69** 115216
- [7] Klochikhin A A, Davydov V Yu, Emtsev V V, Sakharov A V, Kapitonov V A, Andreev B A, Lu H and Schaff W J 2005 *Phys. Rev. B* **71** 195207
- [8] Goldhahn R, Scheiner J, Shokhovets S, Frey T, Köhler U, As D J and Lischka K 2000 *Appl. Phys. Lett.* **76** 291
- [9] Rinke P, Scheffler M, Qteish A, Winkelkemper M, Bimberg D and Neugebauer J 2006 *Appl. Phys. Lett.* **89** 161919
- [10] Furthmüller J, Hahn P H, Fuchs F and Bechstedt F 2005 *Phys. Rev. B* **72** 205106
- [11] Persson C and Ferreira da Silva A 2007 *J. Cryst. Growth* **305** 408
- [12] Lima A P, Tabata A, Leite J R, Kaiser S, Schikora D, Schöttker B, Frey T, As D J and Lischka K 1999 *J. Cryst. Growth* **201–202** 396
- [13] Nishida K, Kitamura Y, Hijikata Y, Yaguchi H and Yoshida S 2004 *Phys. Status Solidi b* **241** 2839
- [14] Nakamura T, Iida K, Katayama R, Yamamoto T and Onabe K 2006 *Phys. Status Solidi b* **243** 1451
- [15] Schörmann J, As D J, Lischka K, Schley P, Goldhahn R, Li S F, Löffler W, Hetterich M and Kalt H 2006 *Appl. Phys. Lett.* **89** 261903
- [16] Schley P *et al* 2008 *Phys. Status Solidi c* at press
- [17] Vurgaftman I and Meyer J R 2001 *J. Appl. Phys.* **89** 5815
- [18] Cimalla V, Pezoldt J, Ecke G, Kosiba R, Ambacher O, Spieß L, Teichert G, Lu H and Schaff W J 2003 *Appl. Phys. Lett.* **83** 3468
- [19] Bagayoko D, Franklin L and Zhao G L 2004 *J. Appl. Phys.* **96** 4297
- [20] Goldhahn R, Shokhovets S, Scheiner J, Gobsch G, Cheng T S, Foxon C T, Kaiser U, Kipshidze G D and Richter W 2000 *Phys. Status Solidi a* **177** 107
- [21] Goldhahn R *et al* 2006 *Phys. Status Solidi a* **203** 42
- [22] Shokhovets S, Goldhahn R, Gobsch G, Piekh S, Lantier R, Rizzi A, Lebedev V and Richter W 2003 *J. Appl. Phys.* **94** 307
- [23] Goldhahn R, Buchheim C, Schley P, Winzer A T and Wenzel H 2007 *Nitride Semiconductor Devices: Principles and Simulation* ed J Piprek (Weinheim: Wiley) p 95
- [24] Kukharskii A A 1973 *Solid State Commun.* **13** 1761
- [25] Kasic A, Schubert M, Einfeldt S, Hommel D and Tiwald T E 2000 *Phys. Rev. B* **62** 7365
- [26] Kaczmarczyk G *et al* 2000 *Appl. Phys. Lett.* **76** 2122
- [27] Hasselbeck M P and Enders P M 1998 *Phys. Rev. B* **57** 9674
- [28] Ishitani Y, Ohira T, Wang X, Che S-B and Yoshikawa A 2007 *Phys. Rev. B* **76** 045206
- [29] Wu J, Walukiewicz W, Shan W, Yu K M, Ager J W III, Haller E E, Lu H and Schaff W J 2002 *Phys. Rev. B* **66** 201403
- [30] Vurgaftman I and Meyer J R 2003 *J. Appl. Phys.* **94** 3675
- [31] Kane E O 1957 *J. Phys. Chem. Solids* **1** 249
- [32] Kamińska A *et al* 2007 *Phys. Rev. B* **76** 075203
- [33] Wu J, Walukiewicz W, Shan W, Yu K M, Ager J W III, Li S X, Haller E E, Lu H and Schaff W J 2003 *J. Appl. Phys.* **94** 4457
- [34] Briki M, Zaoui A, Boutaiba F and Ferhat M 2007 *Appl. Phys. Lett.* **91** 182105